Supporting Information:

Coexistence of ferromagnetism and charge density waves in monolayer $LaBr_2$

Jun Zhou[1], Zishen Wang,[2] Shijie Wang[1], Yuan Ping Feng[2,3*], Ming Yang[4*], Lei Shen[5*]

[1] *Institute of Materials Research & Engineering, A*STAR (Agency for Science, Technology and Research), 2 Fusionopolis Way, Innovis, Singapore 138634, Singapore*

[2] *Department of Physics, National University of Singapore, Singapore 117551, Singapore*

[3] *Center for Advanced Two-Dimensional Materials (CA2DM), National University of Singapore, Singapore 117546, Singapore*

[4] *Department of Applied Physics, The Hong Kong Polytechnic University, Hung Hom, Kowloon, Hong Kong SAR, China*

[5]*Department of Mechanical Engineering, National University of Singapore, Singapore 117575*

*phyfyp@nus.edu.sg

*mingyang@polyu.edu.hk

*shenlei@nus.edu.sg

1. Stability of T' $LaBr_2$ monolayer

The bulk H-phase $LaBr_2$ has been experimentally synthesized while there is no experimental report on the T' phase yet. However, our molecular dynamic simulation shows a small energy variation of T' $LaBr_2$ monolayer (within 0.03 eV/atom) during the heating at 300 K and its 1D-chain like CDW distortions are well-preserved after the heating for 6 ps (see Figure S1). These results indicate the thermal stability of T' $LaBr_2$. Besides, the phonon spectrum shown in Figure 1c demonstrates its dynamic stability. The energy above hull of T'-$LaBr_2$ monolayer was calculated to be 48 meV/atom, which is within the range of the thermodynamic stability for synthesizable materials.[1, 2] It is also noteworthy that the energy difference between the T' and H phases of 42 meV/atom for $LaBr_2$ is much lower than that for most transition metal dichalcogenides (TMDs).[3] And interestingly, the experimental growth of the large-scale and high-quality T' metastable TMDs has been recently reported.[4] Our simulations also show that the T' phase becomes the ground state for an electron doping concentration larger than 0.19 electron per formula unit, which can be achieved experimentally by electrostatic gating [5]. Thus, we expect T'-$LaBr_2$ to be highly feasible for experimental synthesis.

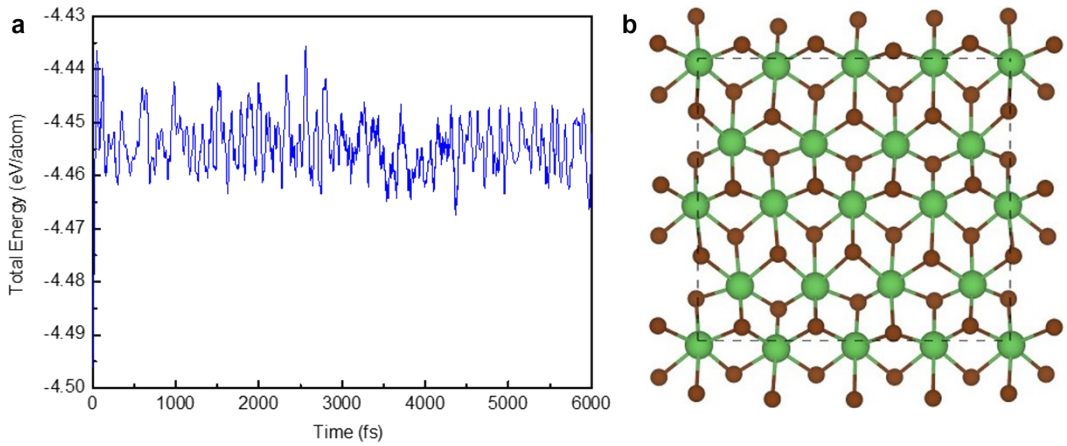

Figure S1. (a) Time-dependent variation of total energies of T' $LaBr_2$ in the molecular dynamics simulation at 300 K. (b) The structure of T' $LaBr_2$ after heating for 6 ps at 300 K.

2. Electride nature of T' $LaBr_2$ monolayer

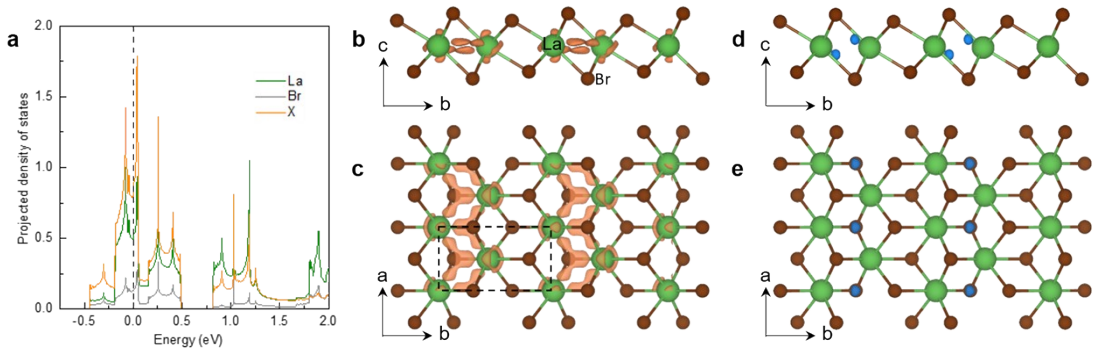

Figure S2. (a) The projected density of states on La, Br, and anionic electron site (denoted by X) of the T' $LaBr_2$ without spin polarization. The Wigner-Seitz radii of La and X are set to half of their distance, while the one for Br is from the default value in the pseudopotential. (b) Side and (c) top view of T' $LaBr_2$ structure with anionic electron band decomposed charge density (isosurface value = 8×10^{-3} $e^-/Å^3$) in orange. (d) Side and (e) top view of T' $LaBr_2$ structure with electron localization function (isosurface value =0.6) in blue.

The electride nature of T' $LaBr_2$ can be shown from different aspects. As discussed in the main article, the anionic electrons do not occupy atomic orbitals and form isolated bands that are well separated from other states [see Figure 2b in the main article]. The isolated state can also be found around the Fermi level in the projected density of states (PDOS), which is mainly contributed by the anionic electron X (thus can be called the anionic electron band) (see Figure S2a). And the anionic electron band decomposed charge density shown in Figure S2b and c mainly distributes on the anionic electron sites. The electron localized function also shows the one excess electron per formula unit in T' $LaBr_2$ localizes on the interstitial site (see Figures. S2d and e). All these results clearly indicate the electride nature of T' $LaBr_2$.

3. Fermi surface nesting

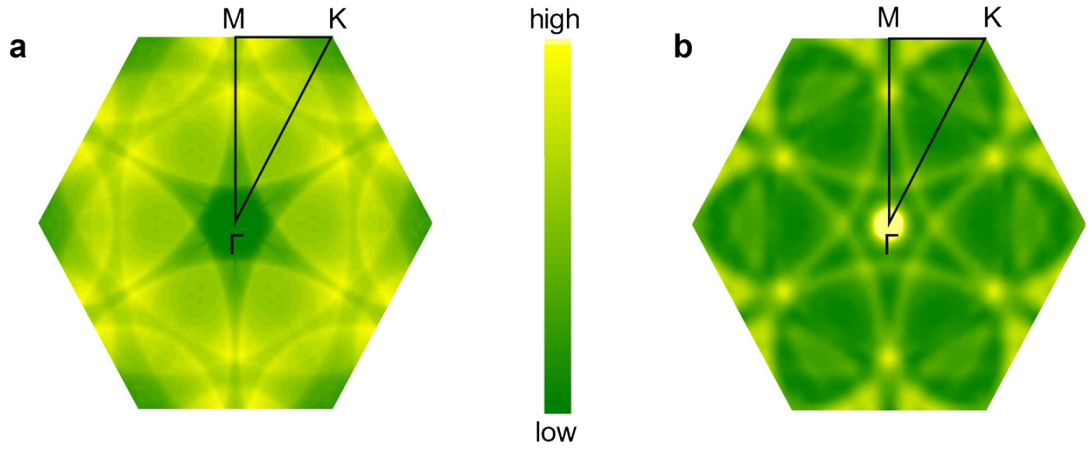

Figure S3. (a) Real and (b) imaginary part of the electronic susceptibility $\chi(q)$, repetitively.

To study the contribution of Fermi surface nesting to the CDW in T $LaBr_2$, the real and imaginary parts of the electronic susceptibility are calculated as follows.

$$\chi_r(q) = \int_{BZ} \frac{dk}{\Omega_{BZ}} \frac{f(\varepsilon_k) - f(\varepsilon_{k+q})}{\varepsilon_{k+q} - \varepsilon_k} \#(1)$$

$$\chi_i(q) = \int_{BZ} \frac{dk}{\Omega_{BZ}} \delta(\varepsilon_k - \varepsilon_F)\delta(\varepsilon_{k+q} - \varepsilon_F) \#(2)$$

where Ω_{BZ} is the area of the first Brillouin zone; $\chi_r(q)$ and $\chi_i(q)$ are the real and imaginary part of electronic susceptibility at phonon momentum **q**; ε_k and ε_F are the band energy at electron moment **k** and Fermi energy; δ is the delta function; respectively. The imaginary part $\chi_i(q)$ is a direct measurement of Fermi surface topology and forms peaks at the nesting vectors [6]. The real part $\chi_r(q)$ takes in account of the hidden nesting conditions around the Fermi surface and reflect the overall electronic instability [7]. As shown in Figures. S3a and b, neither the real nor imaginary parts show the corresponding peak at **M** point as suggested by the position of imaginary

phonon frequencies in Figure 1b of the main text, indicating the unsuitability of the Fermi surface nesting for T-phase $LaBr_2$.

4. Partial charge density for the Mo d^2 electrons in T' MoS_2 monolayer

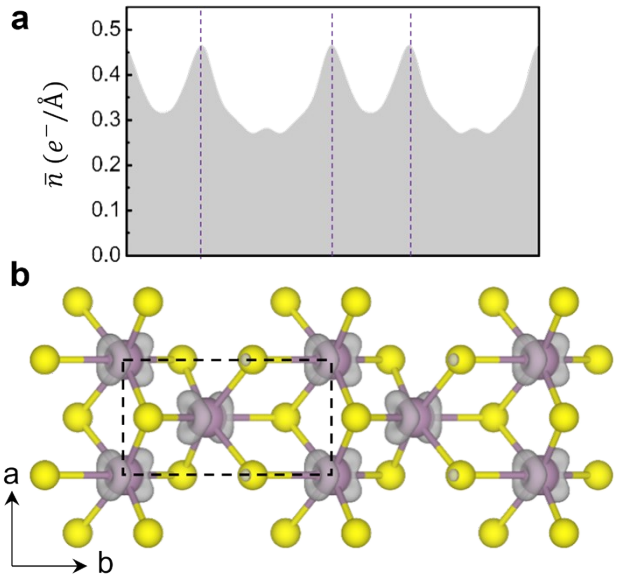

Figure S4. Partial charge density for the Mo d^2 electrons (a) by planer average along *b* axis and (b) by 3D visualization in grey (isosurface value = 1.6×10^{-2} e^-/ Å^3) for T' MoS_2. The purple vertical dash lines in (a) denote the corresponding positions of Mo ions in (b). The yellow and purple balls in (b) represent the S and Mo atoms, respectively.

For a fair comparison between the partial charge density for La d^1 electron in T' $LaBr_2$ and Mo d^2 electrons in T' MoS_2, we divide the planer averaged partial charge of T' MoS_2 by two and set its isosurface value of the 3D visualization to twice of that for T' $LaBr_2$. As shown in Figure S4, the Mo d^2 electrons in T' MoS_2 have stark different distribution with that of the $5d^1$ electrons of La in T-phase $LaBr_2$. Their peaks locate at the Mo positions, demonstrating a traditional charge modulation within the atomic orbitals.

5. Anionic electron bands by DFT and MLWF

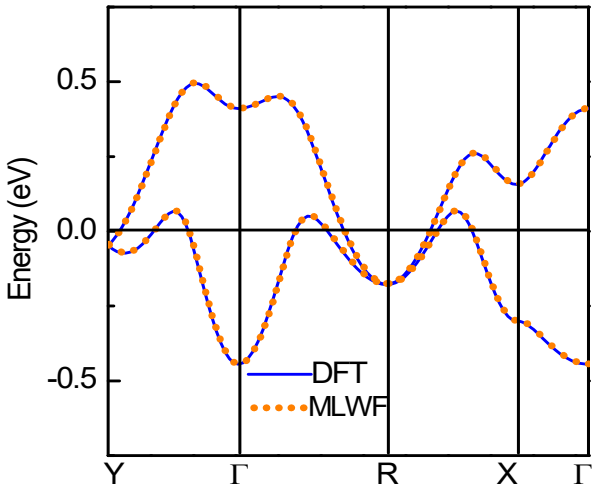

Figure S5. The comparison between the DFT calculated and maximally localized Wannier functions fitted anionic electron bands for T' $LaBr_2$.

The good match between the DFT simulated and MLWF fitted anionic electron bands indicates the high quality of the constructed MLWFs. The real-space visualization of the MLWF (Figure 4b in main text) captures the dual nature of anionic electrons with extended tails around the well-localized body.

6. Phase transition by in-plane biaxial strains

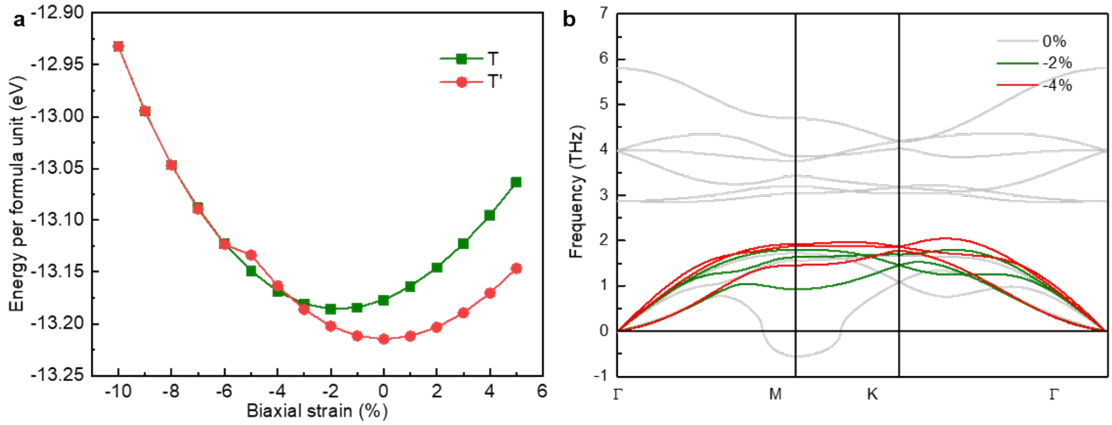

Figure S6. Biaxial strain dependent (a) total energy of the T and T' $LaBr_2$ and (b) phonon band structure of T $LaBr_2$. It is noted the T phase lattices in (a) are deduced from the T' structure in each strain by keeping their in-plane area by a ratio of 2 for a direct comparison. For clarity, only acoustic phonon modes are shown in (b) for T $LaBr_2$ with strain.

It is interesting to note that the CDW structure has very different electronic and magnetic properties from the pristine T $LaBr_2$, which is ideal for nonvolatile applications based on structural phase transition. To explore such capacity, we studied the strain effects on the energy diagram of the T and T' $LaBr_2$. In the pristine form, the T' phase has lower energy than the T phase. However, the structural phase transition from T' to T $LaBr_2$ is possible by applying a biaxial compressive strain of 4%, as shown in Figure S6a. It is also interesting to note that the two curves overlap after the compressive strain is larger than 5%. This can be understood by the strain-dependent energy curve of T' $LaBr_2$ (red curve in Figure S6a), which deviates from a conventional parabola shape but has a sudden drop after the compressive strain is larger than 5%. Such a drop suggests a spontaneous relaxation of the T' $LaBr_2$ to the high-symmetry T structure under a higher compressive strain, which is confirmed by the negligible distance difference between the neighboring La atoms along *b* axis in these optimized structures. Overall, Figure S6(a) illustrates that the T' phase is more stable than the T phase within a bi-axial strain range of -3% to 5%, whereas the T phase becomes more stable for compressive strains larger than -4%. Interestingly, beyond a bi-axial

compressive strain of -5%, the T' phase ceases to exist. This implies that the coexistence of magnetism and CDW can be sustained under strains ranging from -3% to 5% but disappears for compressive strains exceeding -4%.

A useful structural phase transition requires that both phases are stable. In the group VI TMD, the transition is between the H and T' phases as the T structure is metastable. The spontaneous transition from T' $LaBr_2$ to T phase under high compressive strain suggests the latter may be stabilized by strain effects. As shown in Figure S6b, the phonon band structures of T $LaBr_2$ do show a phonon spectrum hardening under compressive strains. The acoustic phonon dip at high-symmetry **M** point widens and shifts to higher energy with compressive strain and becomes positive under a biaxial strain of 2% and disappears when the strain reaches 4%. A similar compressive strain suppressed CDW was shown in monolayer T $TiSe_2$. [8]

7. Relation between CDW and magnetism

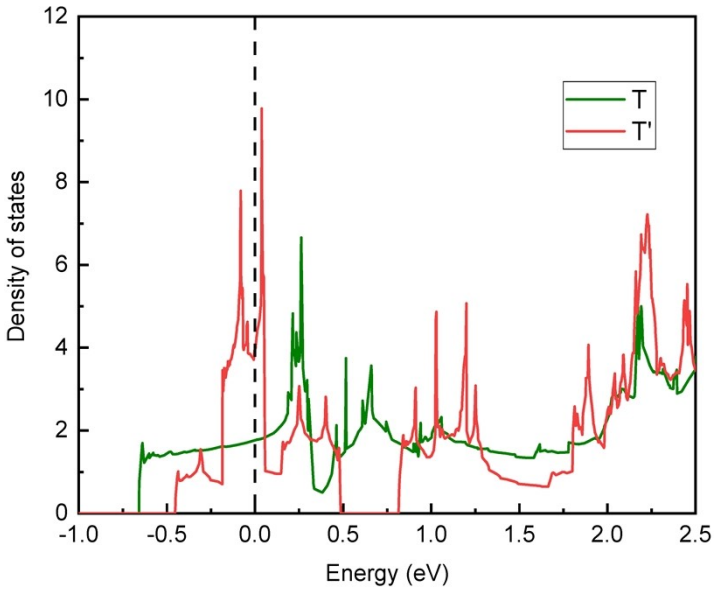

Figure S7. Comparison of the total density of states per formula unit between T and T' $LaBr_2$.

CDW distortions are known to open CDW gaps around the Fermi level, which decreases the density of states at the Fermi level. [9] On the contrary, a high density of states at the Fermi level is needed for spin splitting according to the Stoner model. Thus CDW and magnetism are competing phases and the coexistence of them are rare [10]. However, in the system studied in this work, an opposite trend is observed. As shown in Figure S7, the 2×1 CDW distortions increase the density of states at the Fermi level. Using the Hubbard U and J by cRPA, we obtain a Stoner parameter of 0.338 for the T' $LaBr_2$ by adopting the estimation proposed in ref. [11]. Taking the density of states for T' $LaBr_2$ at Fermi level of 3.97, its product with Stoner parameter is estimated to be 1.34, which is larger than 1, meeting the Stoner criterion for the spontaneous spin splitting in the T' $LaBr_2$. The increased DOS can be understood by the formation of the isolated anionic electron band around Fermi level in the T' $LaBr_2$, in contrast with the wide threefold degenerate t_{2g} bands in the T phase (see Figure 2 of main text).

8. Bilayer and bulk T' $LaBr_2$

To study the effect of the dimensionality increase on the magnetic electride nature of T' $LaBr_2$, we performed simulations for the bilayer and bulk T' $LaBr_2$. As the spin density for bilayer and bulk T'-phase $LaBr_2$ shown in Figures. S8a, b, d, and e, the magnetic moments localize at the interstitial sites between the dimerized La atoms, indicating the dimensionality increase does not affect the magnetic electride nature of the T'-$LaBr_2$. And the phonon band structures for bilayer and bulk T'-phase $LaBr_2$ shown in Figures. S8c and f suggest their stability.

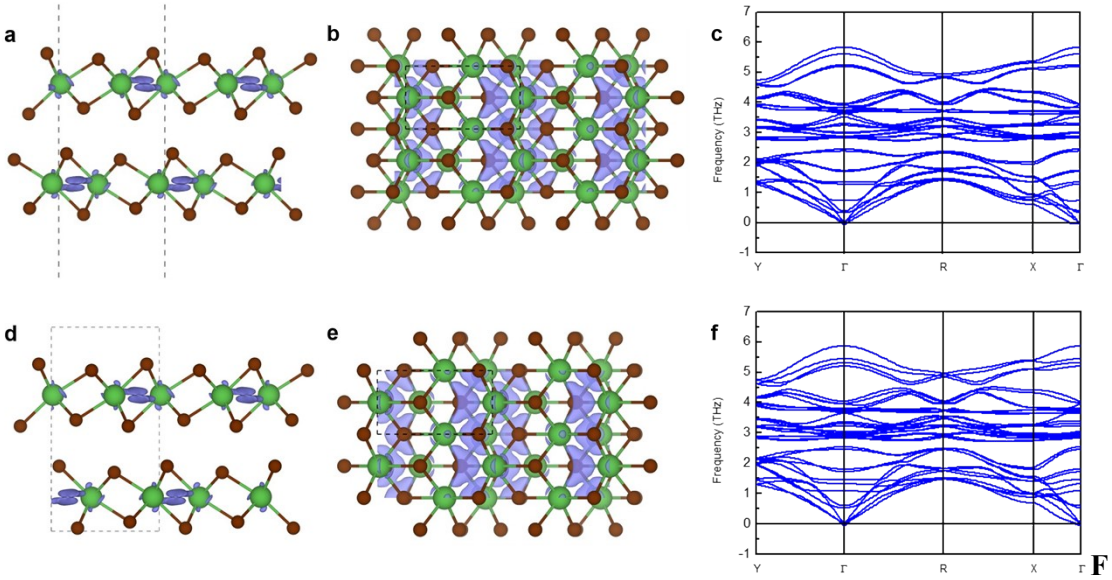

igure S8. The (a) side and (b) top view of the spin density for bilayer T' $LaBr_2$. (c) Phonon band structure for bilayer T' $LaBr_2$. (d)-(f) are the same as (a)-(c) but for bulk T' $LaBr_2$.

9. Band structure of $LaBr_2$ with spin-orbital coupling

As shown in Figure S9, the spin-orbital coupling (SOC) has negligible effects on the electronic properties of T' $LaBr_2$, especially for the two anionic electron bands crossing the Fermi level. This is also reflected by fact that the inclusion of SOC does not change the total magnetic moment of 0.93 μ_B/f.u. for T' $LaBr_2$ (at PBE level).

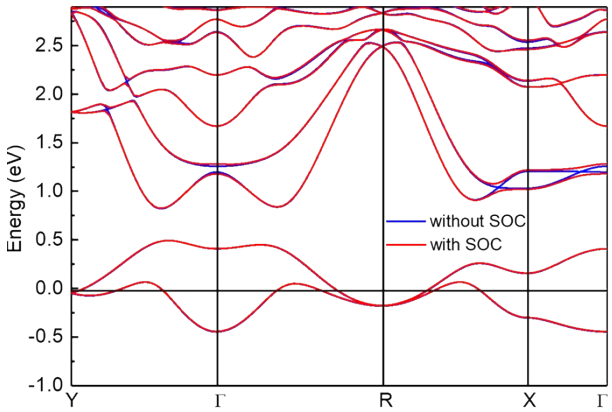

Figure S9. Non-spin-polarized band structure of T' $LaBr_2$ with/without spin-orbital coupling.

10. $LaCl_2$ and LaI_2

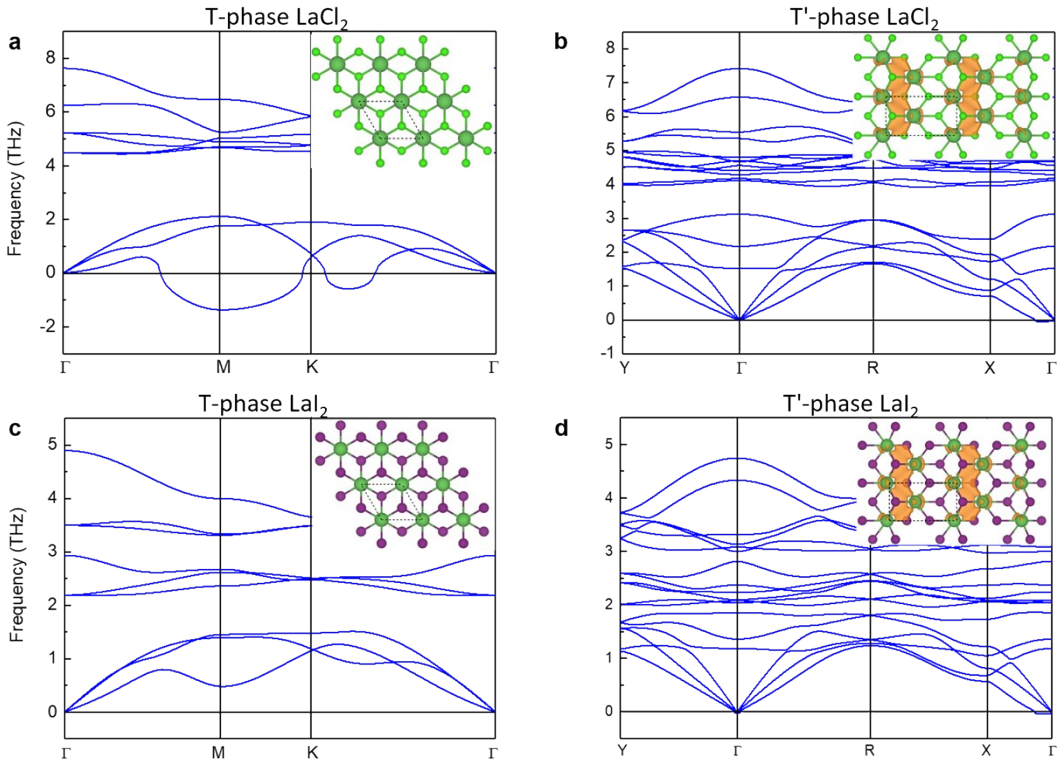

Figure S10. Phonon spectra for (a) T-phase $LaCl_2$, (b) T'-phase $LaCl_2$, (c) T-phase LaI_2 and (d) T'-phase $LaCl_2$. The inset in (a) and (c) is the structure in top view of T-phase $LaCl_2$ and LaI_2, respectively. The insets in (b) and (d) are structures in top view of T'-phase $LaCl_2$ and LaI_2 with spin density (isosurface value = 8×10^{-3} $e^-/Å^3$), respectively.

To investigate the general applicability of the coexistence of magnetism and CDW, we have performed DFT simulations for $LaCl_2$ and LaI_2. As shown in Figure S10, the T-phase of $LaCl_2$ is not stable with imaginary phonons at around **M** point, corresponding to a 2×1 phase transition to T' phase. Besides, the imaginary phonons along the **K-Γ** path suggest the existence of other CDW pattern in $LaCl_2$. Interestingly, the T'-phase $LaCl_2$ is stable both dynamically and energetically (23.70 meV/f.u. lower than the T phase) and the magnetic moments (0.78 μ_B/f.u.) are mainly localized at the interstitial sites [see the spin density distribution in the inset of Fig. S10(b)]. On the contrary, both the T and T' phase of LaI_2 are stable, but the energy of T' phase is 17.20 meV/f.u. lower than that of the T phase. Importantly, the T' phase of LaI_2 is also magnetic with

magnetic moment of 0.99 μ_B/f.u. mainly localized at the interstitial sites [see the spin density distribution in the inset of Fig. S10(d)]. This suggests the co-existence of magnetism and CDW can also be found in $LaCl_2$ and LaI_2. Considering lanthanoid (II) halides are a large group of materials[12], more materials with similar phenomena are expected to exist.

References

1.Z. Wang, I.-H. Chu, F. Zhou and S. P. Ong, *Chem. Mater.*, 2016, **28**, 4024-4031.

2.G. Hautier, A. Jain, S. P. Ong, B. Kang, C. Moore, R. Doe and G. Ceder, *Chem. Mater.*, 2011, **23**, 3495-3508.

3.K. A. Duerloo, Y. Li and E. J. Reed, *Nat. Commun.*, 2014, **5**, 4214.

4.Z. Lai, Q. He, T. H. Tran, D. V. M. Repaka, D. D. Zhou, Y. Sun, S. Xi, Y. Li, A. Chaturvedi, C. Tan, B. Chen, G. H. Nam, B. Li, C. Ling, W. Zhai, Z. Shi, D. Hu, V. Sharma, Z. Hu, Y. Chen, Z. Zhang, Y. Yu, X. Renshaw Wang, R. V. Ramanujan, Y. Ma, K. Hippalgaonkar and H. Zhang, *Nat. Mater.*, 2021, **20**, 1113-1120.

5.I. A. Verzhbitskiy, H. Kurebayashi, H. Cheng, J. Zhou, S. Khan, Y. P. Feng and G. Eda, *Nat. Electron.*, 2020, **3**, 460-465.

6.P. Chen, W. W. Pai, Y. H. Chan, V. Madhavan, M. Y. Chou, S. K. Mo, A. V. Fedorov and T. C. Chiang, *Phys. Rev. Lett.*, 2018, **121**, 196402.

7.M. D. Johannes and I. I. Mazin, *Phys. Rev. B*, 2008, **77**, 165135.

8.M. J. Wei, W. J. Lu, R. C. Xiao, H. Y. Lv, P. Tong, W. H. Song and Y. P. Sun, *Phys. Rev. B*, 2017, **96**, 165404.

9.A. O. Fumega, M. Gobbi, P. Dreher, W. Wan, C. González-Orellana, M. Peña-Díaz, C. Rogero, J. Herrero-Martín, P. Gargiani, M. Ilyn, M. M. Ugeda, V. Pardo and S. Blanco-Canosa, *J. Phys. Chem. C*, 2019, **123**, 27802-27810.

10.K. K. Kolincio, M. Roman and T. Klimczuk, *Phys. Rev. Lett.*, 2020, **125**, 176601.

11.G. Stollhoff, A. M. Oles and V. V. Heine, *Phys. Rev. B*, 1990, **41**, 7028-7041.

12. H. A. Eick, *J. Less-Common Met.*, 1987, **127**, 7.